Analysis of Metal Elements Contained in Graphite Target Coated With Chinese Medicinal Material Nanoparticles Using LIBS

Weiwei Han[1], Yongqiang Wang[1], Yaopeng Yin[2], Xuerui Li[1], Duixiong Sun[1]* and Maogen Su[1]*

[1]Key Laboratory of Atomic and Molecular Physics and Functional Material of Gansu Province, College of Physics and Electronic Engineering, Northwest Normal University, Lanzhou, China, [2]National Ancient Wall Painting and Earthen Archaeological Site Engineering Research Centre, Dunhuang, China

A nanoparticle-coated graphite target (NCGT) is presented to improve the analysis accuracy and stability of laser-induced breakdown spectroscopy (LIBS). A stable, relatively homogeneous, and close to optically thin laser-induced breakdown plasma was obtained by dispersing sample nanoparticles on a high-purity graphite substrate. Spectral structures dominated by the characteristic lines of carbon and the samples can greatly simplify spectral identification and avoid line interference. To maximize the analysis accuracy and stability, a series of experimental conditions were optimized step by step according to the spectral intensity and signal-to-noise ratio of the lines. Based on the final optimized conditions, the relative standard deviation values of Mg, Fe, and Sr elemental content in Chinese medicinal material (CMM) samples were reduced from 17.7, 16.6, 12.1% of the pressed target to 4.8, 9.5, and 4.5% of the NCGT, respectively. Comparisons with the inductively coupled plasma mass spectrometry (ICP-MS) results demonstrated that the present method has great potential for detection of LIBS.

Keywords: laser-induced breakdown spectroscopy, nanoparticle-coated graphite target, Chinese medicinal material, metal elements, plasma parameters

INTRODUCTION

In recent decades, there has been a burst of enthusiasm for the fundamental studies of laser-induced breakdown spectroscopy (LIBS) and its applications to many analytical fields because of its advantages of limited sample preparation, multi-elemental analysis, and its capability for remote and *in-situ* analysis of materials in any phase [1–3]. Benefit from the advantages of sensitive and rapid spectral technology [4–7], LIBS as a rapid analytical tool with great potential for determining the elemental composition of materials in the solid, liquid, and gaseous states, many investigations on the spectral stability [8, 9], data processing [10, 11, 12] have recently been developed and reported. Several techniques have been proposed for enhancing the sensitivity of LIBS like Double pulse LIBS [13], resonance LIBS [14], the use external electric or magnetic field [15, 16] and LIF-LIBS, but all these techniques require the use of an additional energy source or tunable lasers. On the contrary, Nanoparticle Enhanced LIBS just requires a minimum sample preparation that is the deposition of nanoparticle on the sample surface [17, 18]. Nevertheless, so far only few investigations have focused on the effect of this phenomenon due to the influence of various factors such as matrix effect.

FIGURE 1 | Schematic of LIBS and sample target preparation. **(A)** Dispersed particles from LIBS, **(B)** TEM image of nanoparticle suspensions, **(C)** the image of ablated NCGT surface at the power density of 1.5×10^9 W/cm^2.
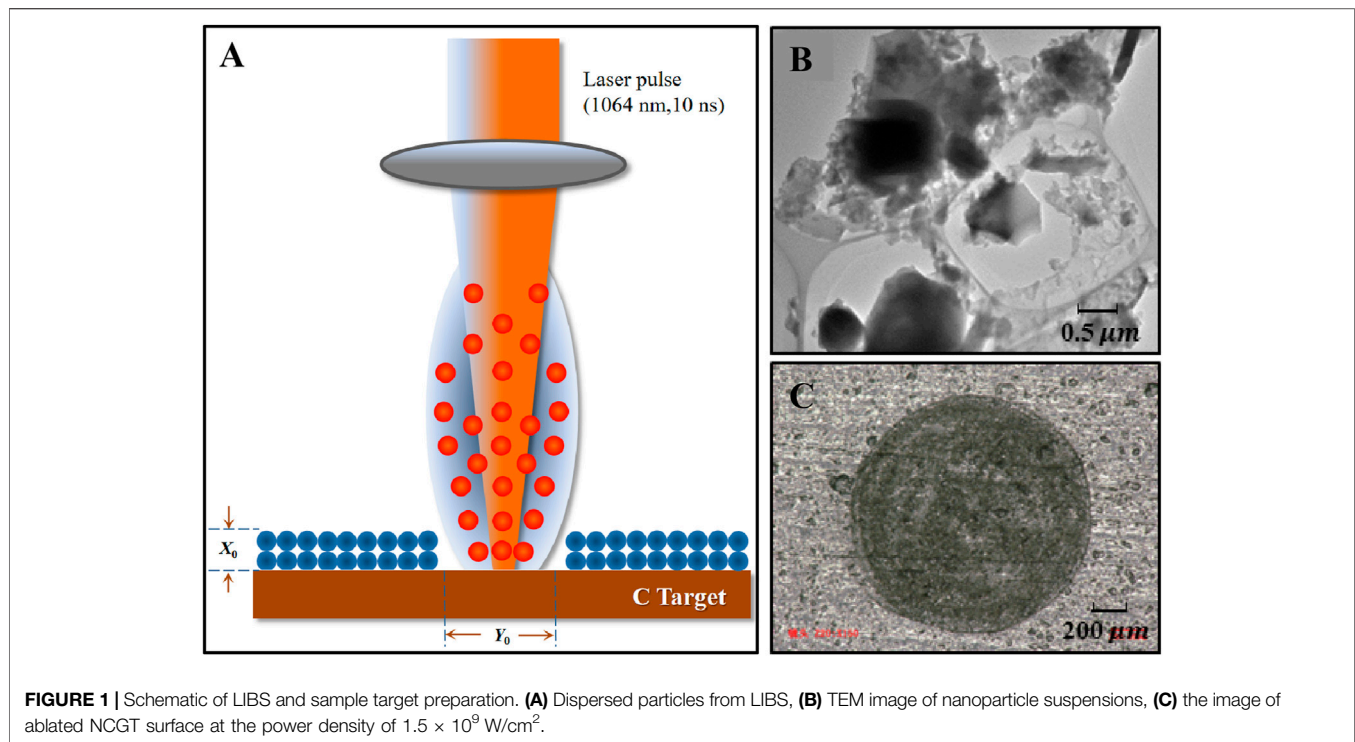
A key issue for accurate determination of trace elements in samples is to create a stable, close to optically thin, and relatively homogeneous plasma environment [19]. LIBS investigations have shown that most of the current mature laser and spectral detection instruments meet the requirements of LIBS detection with regards to stability and sensitivity [20], and high precision timing-control and detection-location [21] can easily assist in determining the optimized experimental conditions. However, for most LIBS spectroscopic measurements, two important factors affecting the instability of the spectral signal are the inhomogeneous distribution of the material on a target surface and the unevenness of the sample target surface [22, 23]. These two factors can result in the intensity and shape of the lines exhibiting unreasonable oscillations for some sensitive characteristic emission lines because of pulse-to-pulse fluctuations, for example, Mg II lines at 279.55 and 280.27 nm, and Ca II lines at 393.36 and 396.84 nm. Especially, self-absorption or self-reversed profiles may be observed in extreme cases.

Therefore, a suitable substrate for trace elements is necessary to improve the performance of LIBS detection. A high-purity graphite target could be considered as a kind of ideal substrate because of its simple spectral structure and hexagonal layered structure. As one of the most common elements, elemental carbon has the simplest spectral structure compared with other elements in the range 200–425 nm, exhibiting only an isolated resonance line at 247.86 nm and three CN molecular bands near 358 nm, 388.3 nm, and 421.6 nm. These features greatly simplify spectral identification. Meanwhile, the inherent

compact nature of graphite can keep plasmas sufficiently stable during laser ablation so as to effectively enhance the spectral stability. Thus, a high purity graphite target is an excellent candidate for high precision LIBS investigations.

Another method to create an optically thin and relatively homogeneous plasma is by coating a small amount of sample onto the high purity graphite target surface as evenly as possible. Nanoparticles obtained by the ashing method could be an attractive choice since their small sizes enable a thin and even coating on the surface. And the main contents including metal elements were kept while a lot of C, H and O elements were burned in the ashing process, which further reduce the line identifications. One can expect that only sample nanoparticles with a thickness of less than 1 μm would be stripped upon low-energy laser pulse ablation. Therefore, such a plasma would be dominated by content originating from the graphite target while only a very small amount of content is from the sample.

In this work, a high purity graphite target was chosen to improve the stability of plasmas and to investigate the feasibility and capacity in Nanoparticle Enhanced LIBS detection. A traditional Chinese medicinal material (CMM) was specially selected as the analytical sample because of its therapeutic effects [24–26]. Laser-induced breakdown spectroscopy based on the nanoparticle-coated graphite target (LIBS-NCGT) was studied from the fundamental and application points of view. Our aim is to develop an analytical procedure to promote analysis efficiency of elements contained in the CMM samples based on the high-purity graphite targets.
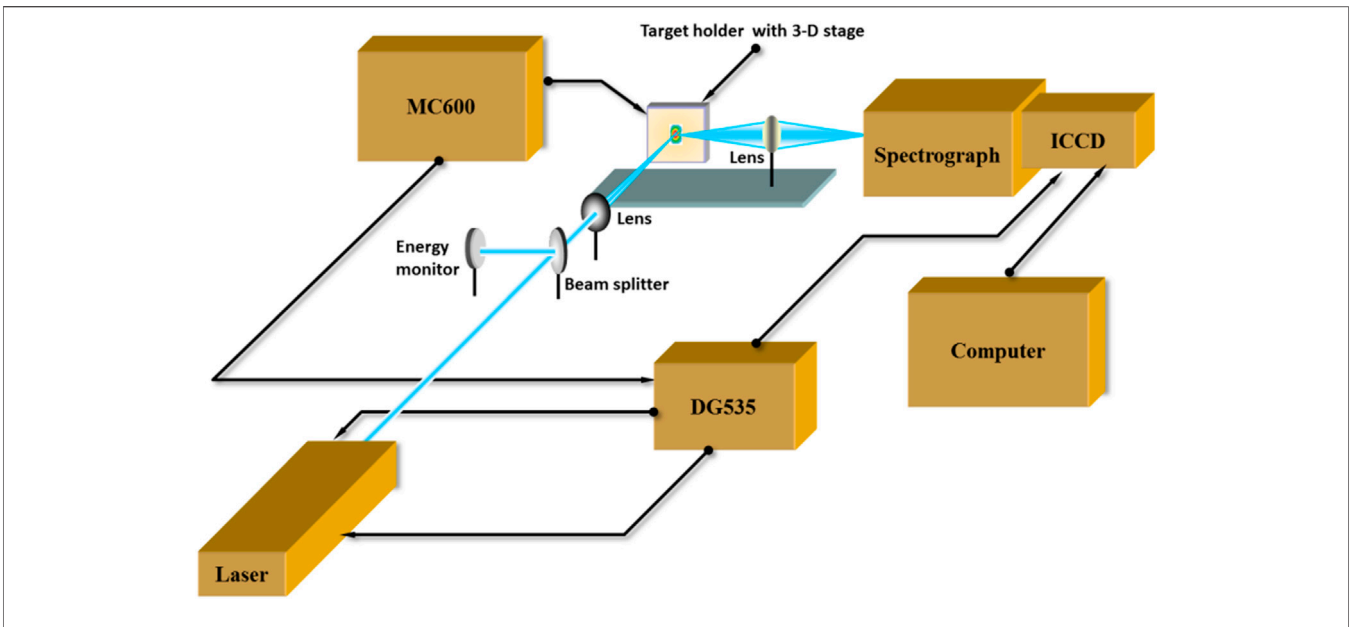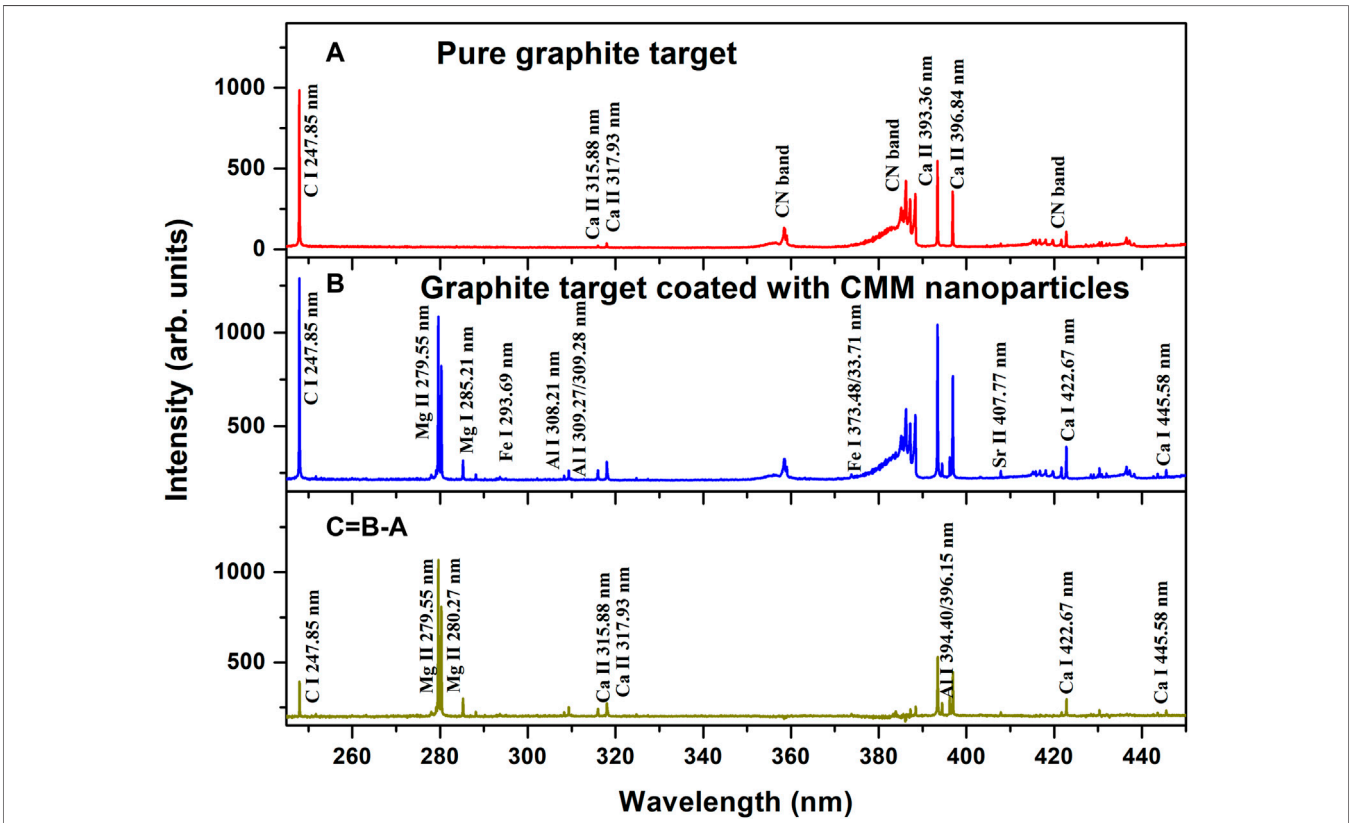
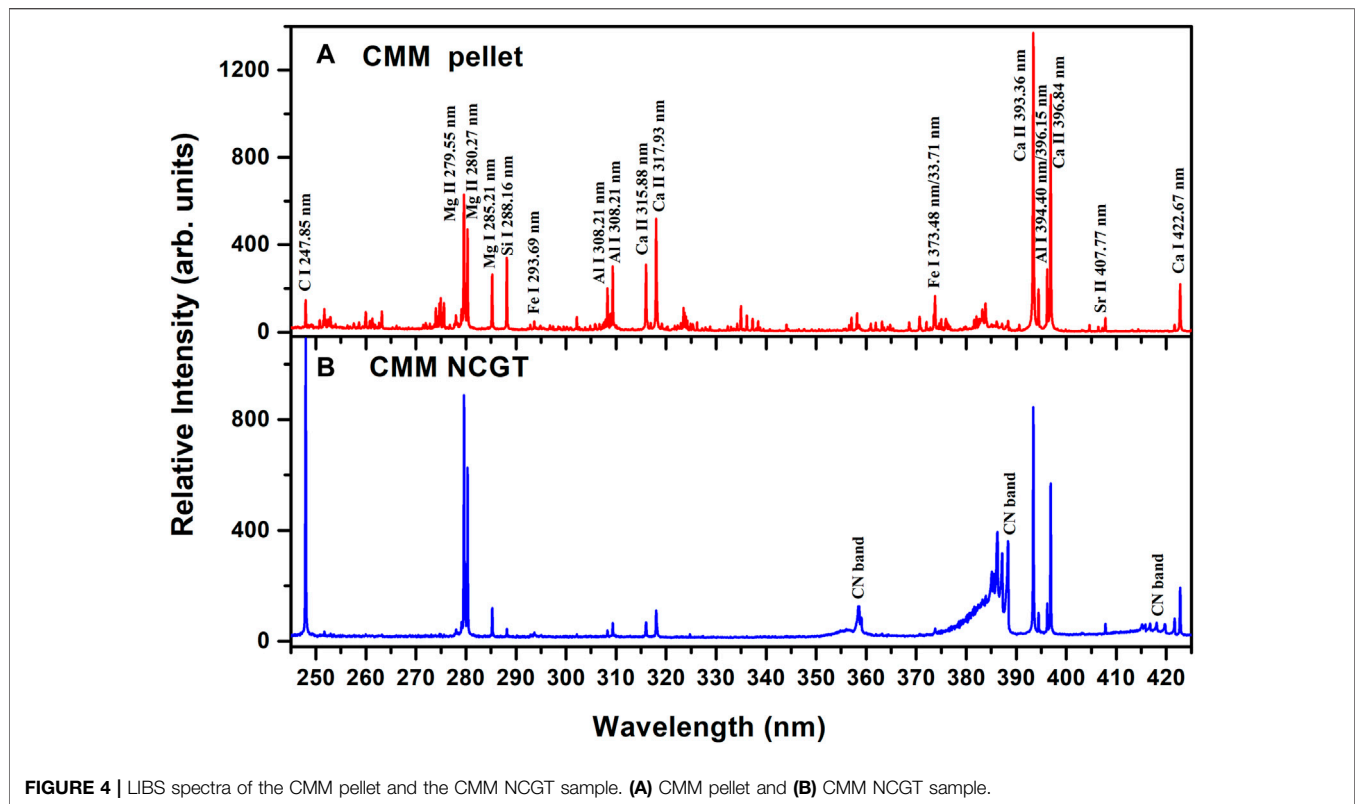**FIGURE 2 |** Schematic of the experimental setup.

FIGURE 3 | LIBS spectra of the graphite target and the CMM NCGT. **(A)** Pure graphite target, **(B)** CMM NCGT sample, and **(C)** the result of **(B)**-**(A)**.

FIGURE 4 | LIBS spectra of the CMM pellet and the CMM NCGT sample. **(A)** CMM pellet and **(B)** CMM NCGT sample.

EXPERIMENTAL

Methods

A nanoparticle-coated graphite target (NCGT) was designed by coating sample nanoparticles onto a high purity graphite target surface, which was several microns in thickness and was sufficiently uniform in distribution. When a focused laser pulse ablates a target surface, a laser-induced breakdown plasma including massive graphite composition and trace sample composition will be produced. **Figure 1A** shows the diagram of dispersed particles from a laser-induced breakdown plasma. Here, the matrix effect of the graphite substrate is expected to be helpful to stabilize the plasma signal and reduce the interference of spectral lines. A uniformly distributed nanoparticle film coated on the graphite substrate can provide adequate sample species after ablation, and these species interact with carbon ions from graphite substrate in the plasma expansion so as to prominent the signals of sample composition.

Sample Target Preparation

A planar high-purity graphite (purity>99.999%) target was chosen as a substrate to carry the sample nanoparticles to be measured.
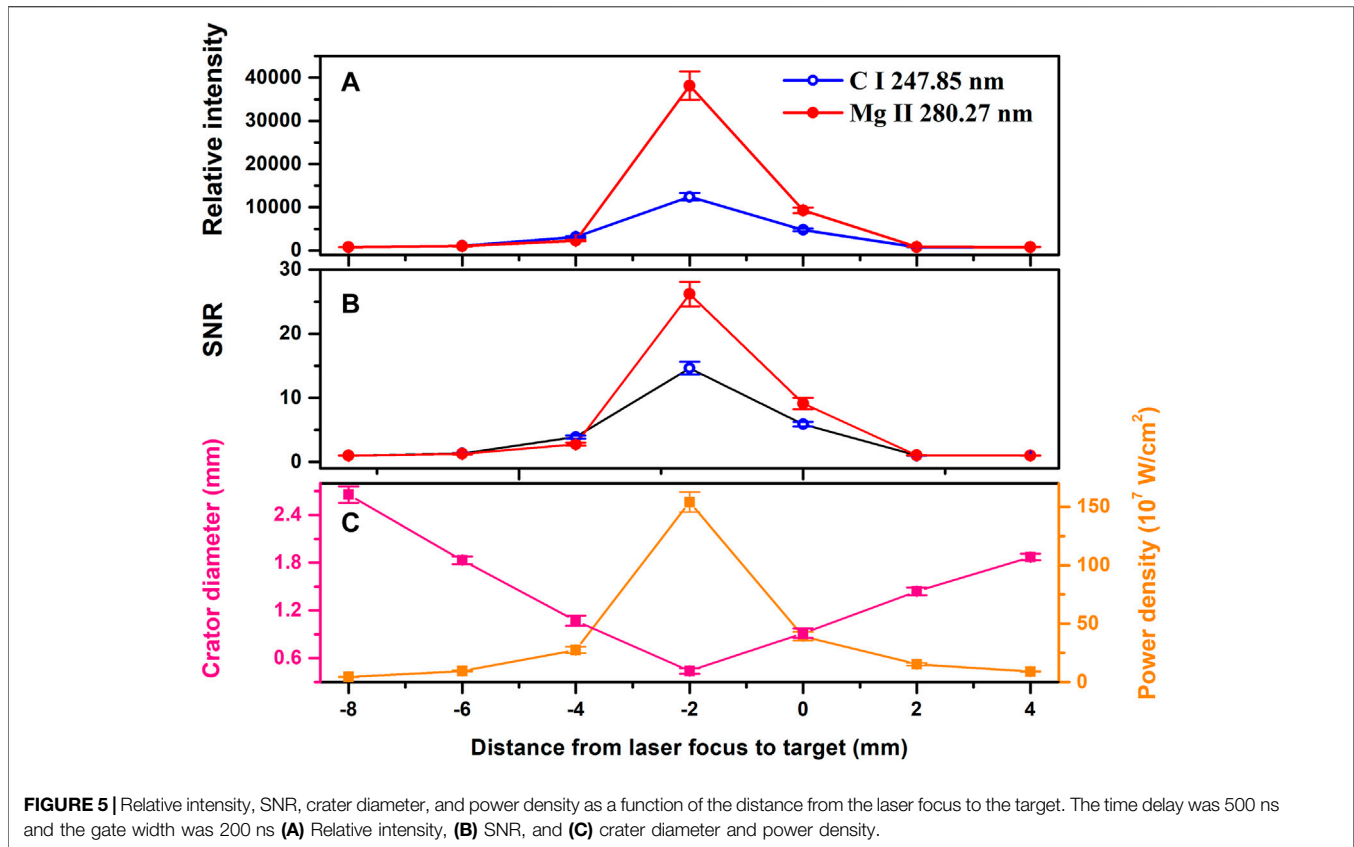
Codonopsis pilosula samples, produced in Ming County, Gansu, China, were prepared, which belongs to a perennial species of flowering plant in the bellflower family. Their root

materials were chosen as sample and placed in an electric constant temperature drying box to dry for 40 min at 60°C, and were then transferred to an analytical grinding machine for grinding. These powders were filtered using a 300-mesh sieve. Powder samples (1.0 g) were weighed and then were pressed to pellet with a 20 mm diameter and a 2.5 mm thickness. Pellets of pure CMM were prepared for comparison.

Dry powder samples (5.0 g) were placed in a crucible and heated for 40 min, until the sample no longer released smoke, for regulated electric heating carbonization, and then placed into a muffle furnace to ash for 8 h at 600°C so that a white ash was produced after cooling in the muffle furnace.

The ash in the crucible was dissolved in analytical-grade ethanol, and then transferred to a 50 ml volumetric flask for ultrasonication for 60 min with an ultrasonic cleaning instrument (KQ-3200E) to produce a suspension.

Large numbers of nanoparticles having diameters of tens to several hundred nanometers were imaged with transmission electron microscopy (TEM), as shown in **Figure 1B**. The nanoparticle suspensions were uniformly coated on the graphite surface. After evaporation of the ethanol, the nanoparticles were evenly distributed on the graphite substrate. This was called the nanoparticle-coated graphite target (NCGT). **Figure 1C** shows the image of an ablated NCGT surface at the laser power density of $1.5 \times 10^9 \, \text{W/cm}^2$, the ablation had a diameter of 0.5 mm.

FIGURE 5 | Relative intensity, SNR, crater diameter, and power density as a function of the distance from the laser focus to the target. The time delay was 500 ns and the gate width was 200 ns **(A)** Relative intensity, **(B)** SNR, and **(C)** crater diameter and power density.

EXPERIMENTAL

A schematic of the experimental setup is shown in **Figure 2**. A 1064 nm Nd: YAG laser (PRO-350, Spectra-Physics) with a 10 ns pulse width, was used to produce plasmas when focused onto the planar NCGT surface. The target holder was positioned on a three-dimensional translation stage with a resolution of 0.1 mm to enable the presentation of a fresh area for each laser pulse. A lens positioned on a linear translation stage with the same resolution could be moved along the laser beam direction to adjust the focusing. The target and the lens can be moved simultaneously with the same step perpendicular to the normal of the target surface by controlling the translation stages. The space emission from the plasmas was collected with a quartz lens having a 50 mm focal-length onto the entrance slit of a spectrometer (Shamrock SR-500i, Andor technology) equipped with an intensified charge-coupled device (ICCD, iStar-DH734-18F-03, Andor technology). The spectral response of the intensity was calibrated using deuterium and tungsten halogen lamps (Aracight-D-CAL1205001). A digital delay generator (DG535, Stanford) was used to synchronize the laser pulse and the ICCD. Emissions from ten laser pulses were averaged for each measurement. The sample movement and spectral acquisition parameters were computer controlled and the experiments were performed in air at atmospheric pressure. To suppress

background from the continuum plasma radiation and to enhance spectral stabilities, the experimental conditions were optimized step by step.

DISCUSSION

Comparison Between LIBS Spectra of Graphite Target and NCGT CMM Samples

Figures 3A,B plot LIBS spectra of the graphite target and CMM NCGT samples over the wavelength range of 245–450 nm, respectively, which were collected 1.5 mm from the target surface at a laser power density of 1.5×10^9 W/cm^2. The gate-width was 200 ns and the time delay were 500 ns It is clear that the spectral structure of the high purity graphite target in **Figure 3A** was very simple. In particular, there were no interference lines in the 250–357 nm range, except for two very weak Ca II lines at 315.88 and 317.93 nm. There were also three characteristic CN molecular bands around 358 nm, 388.36 nm, and 421 nm. Other peaks could easily be identified as Ca II lines at 393.36 and 396.84 nm, as well as Sr II lines at 407.77 nm. All of the lines were isolated and exhibited good resolution, with a maximum full width at half maximum (FWHM) of less than 0.11 nm. Finally, the rotational tail of the CN molecular band weakly interfered with these lines.

For CMM NCGT, new spectral lines in **Figure 3B** appeared at 279.55, 280.27, 285.21, 308.21, 309.27, 394.40, and
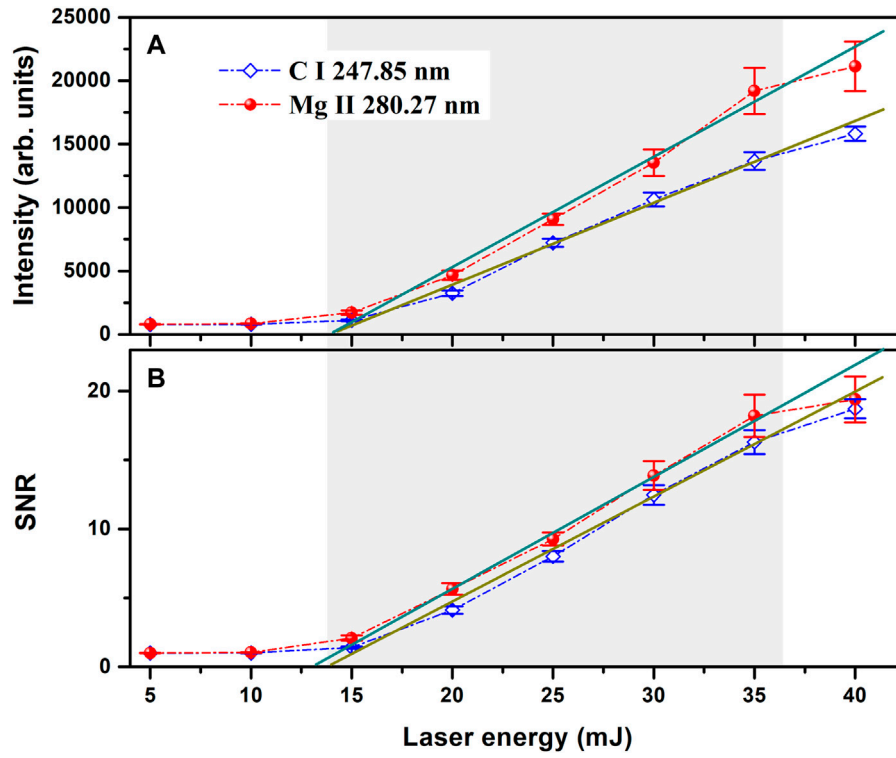
FIGURE 6 | Relative intensity and SNR as a function of laser energy. The time delay was 500 ns, and the gate width was 200 ns **(A)** Relative intensity, **(B)** SNR.
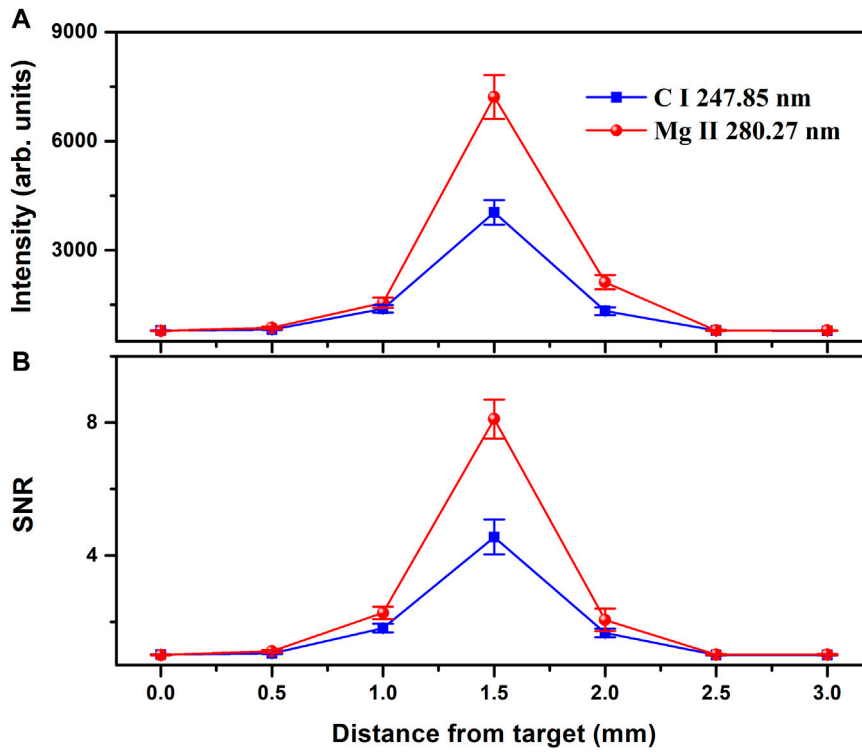

FIGURE 7 | Relative intensity and SNR as a function of detection distance from the target. **(A)** Relative intensity, **(B)** SNR.
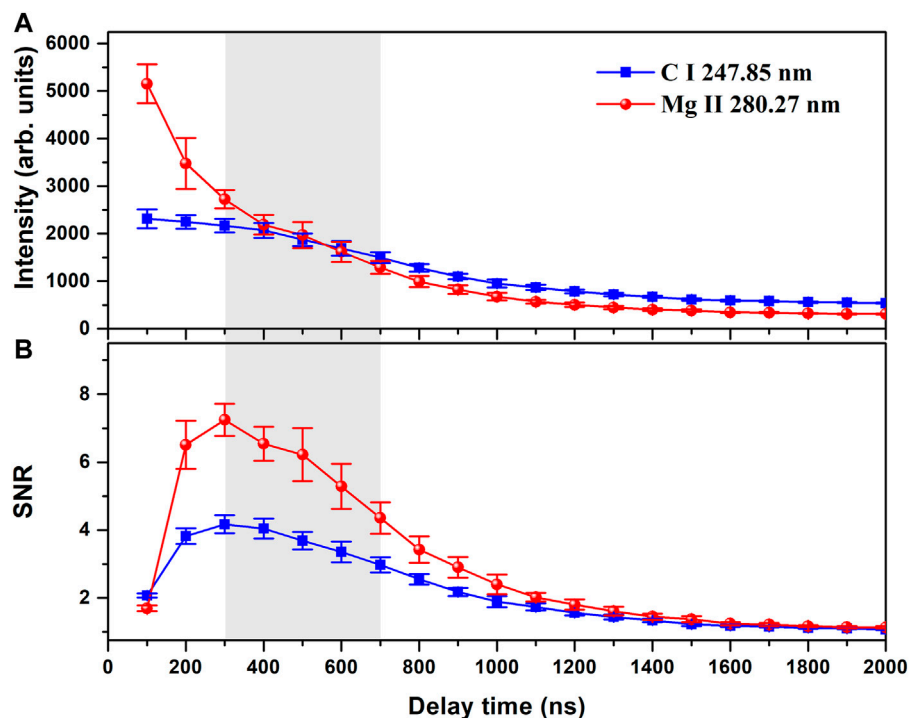
FIGURE 8 | (A) Relative intensity and **(B)**SNR as a function of delay time.
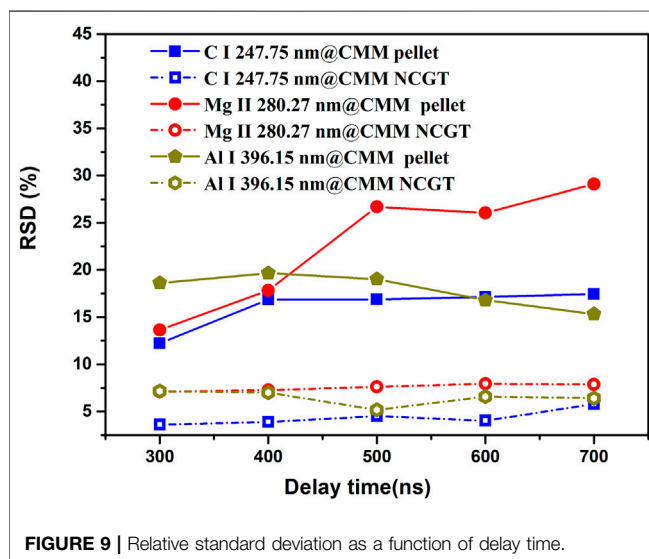

FIGURE 9 | Relative standard deviation as a function of delay time.

396.15 nm, Ca I 422.67 nm, Ca I 445.58 nm, which were respectively identified as Mg II, Al I, and Ca I. Some peaks were enhanced, such as the C I line at 247.85 nm, the Ca II lines at 315.88 and 317.93 nm, and the Ca II lines at 393.36 and 396.84 nm, as well as Sr I line at 407.77 nm. **Figure 3C** shows the result of subtracting spectrum (A) from spectrum (B). The result was contributions from the CMM sample; the graphite features in **Figure 3A** were weak, and the three CN molecular bands disappeared. This indicated that by this treatment, the
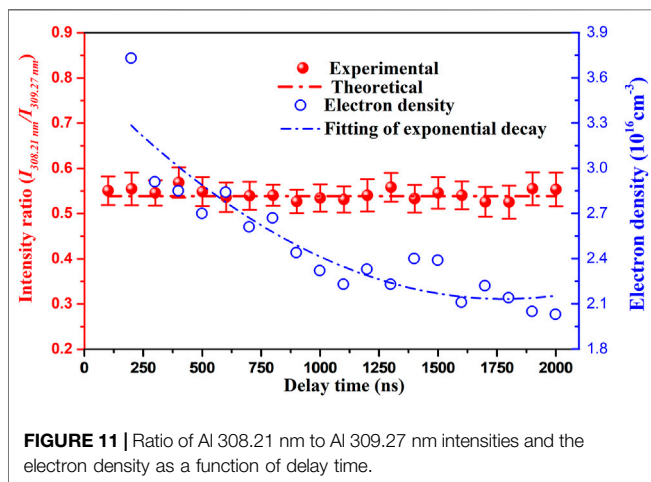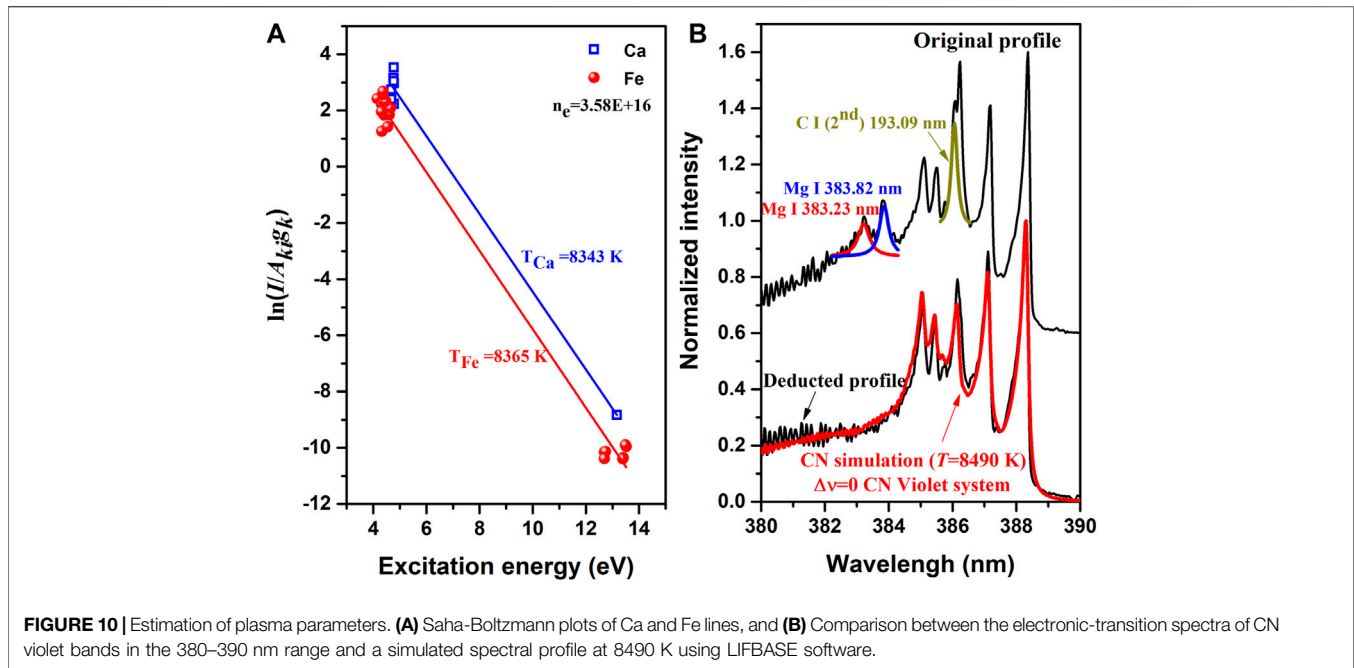
spectra of Chinese herbal medicine nanoparticles can be obtained.

Figure 4A,B allow comparison between the LIBS spectra of pure CMM pellet and the graphite target coated with CMM nanoparticles, respectively. In **Figure 4A**, a total of 248 lines were identified as transitions of C I, Mg II, Si I, Fe I, Ca II, and Sr II ions, in addition to three weak CN bands. In **Figure 4B**, only 29 lines appeared, all of which were characteristic lines from ions mentioned above. Thus, they could be easily and rapidly identified.

Optimization of Conditions

Further optimization of the experimental conditions was very necessary for investigating the NCGT-LIBS detection capacity combined with the graphite substrate and nanoparticle homogeneity. Two analytical lines were selected. One was the C atomic line at 247.85 nm that represented the matrix nature of the graphite target, and the other was the sensitive Mg ionic line at 280.27 nm that represented the sample nanoparticles. Step-by-step optimization included the laser focusing, the laser energy, the detection position, and the time delay. The intensities and signal-to-noise ratios (SNRs) of the lines were used to evaluate the stabilities of the plasma signals and the degree of optimization.

Figure 5 shows the variation of the relative intensity, the SNR, diameter of the ablated crater, and the power density as a function of distance from laser focus to target. The movement range of the focus point was −8–4 mm from the target surface along the laser beam direction. The highest spectral intensity and SNR were at the −2 mm focus point. Here, the diameter of the ablated crater

FIGURE 10 | Estimation of plasma parameters. **(A)** Saha-Boltzmann plots of Ca and Fe lines, and **(B)** Comparison between the electronic-transition spectra of CN violet bands in the 380–390 nm range and a simulated spectral profile at 8490 K using LIFBASE software.

FIGURE 11 | Ratio of Al 308.21 nm to Al 309.27 nm intensities and the electron density as a function of delay time.

was approximately 0.3 mm, the laser power density was approximately 1.55×10^9 W/cm^2, and the corresponding laser energy was 25 mJ.

Under the optimized focusing conditions, line intensities as a function of laser energy were investigated. **Figures 6A,B** respectively plots the relative intensity and SNR values of the lines as a function of laser energy. Both increased with a near-linear trend over the range 15–35 mJ highlighted by the gray rectangular box in **Figure 6**. For clarity, the experimental data were linearly fitted, as displayed by the solid lines with correlation coefficients greater than 98%. When the laser energy was greater than 40 mJ, the intensity and SNR values became weaker because of instrument saturation. This indicated that the plasmas were optically thin, and with the increase of laser energy, the intensity of spectral lines increases linearly in the range 15–35 mJ. To ensure that weak signal was not lost and that

strong signals were not saturated in the following optimizations, a laser energy of 25 mJ was used.

Figure 7 shows the relative intensity and the SNR at a laser energy of 25 mJ as a function of detection distance from the target. The space detection scale of the plasma was approximately 3 mm, and the best spectral signal and SNR values were obtained at 1.5 mm from the target surface. This value was thus fixed in the following optimization.

Figure 8 shows the **(A)** relative intensity and **(B)** SNR as a function of delay time. The spectral intensity rapidly decreased, while the SNR sharply increased initially with delay time, then gradually decreased down to 1 after 2 μs.

Figure 9 plots the relative standard deviation (RSD) of plasma signals for the CMM pellets and CMM NCGT samples for time delays in the range 300–700 ns RSD values of the C I and Mg II lines from the CMM NCGT samples were approximately three times lower than those from the CMM pellets, and were almost constant with increasing time delay. This indicated that the NCGT-LIBS method had good plasma stability for CMM LIBS investigations.

Diagnosis of Plasma Parameters

To investigate the physical property of the plasma based on graphite target coated CMM nanoparticles, the electron density and temperature were determined. The electron density was determined using the Stark broadening method [27]. Specifically, the Ca II line at 396.84 nm was used because of its sensitivity to Stark broadening. The line FWHM was determined by Lorentz fitting, and the electron density was estimated to be 3.58×10^{16} cm^{-3}. The plasma temperature was first deduced using the Saha-Boltzmann plot method [29]. Atomic and ionic lines of Ca and Fe were used to increase the precision of the temperature. **Figure 10A** shows Saha-Boltzmann plots of the two elements. The average plasma

temperature was approximately 8354 K. To check this value, **Figure 10B** shows the comparison between the acquired spectra of electronic-transitions in the CN violet band over the 380–390 nm range, along with a simulated spectrum at 8490 K using LIFBASE software [28]. The software can be used to generate simulated spectra across a broad temperature range at 100 K temperature increments using the Vogit profiles and a spectrometer resolution of 0.05 nm. The black solid line in the lower part of the figure is the result after deducting the contributions of emission lines of Mg I 383.82 nm, Mg I 383.23 nm and a second order emission C I line at 193.09 nm. The result indicated that the intensities across the simulated spectrum matched very well with the deducted experimental profile. Thus, reasonable temperature fits were obtained.

Optical Thickness

For intense atomic lines, such as some carbon and sodium lines from plant materials, self-absorption cannot be neglected. In this case, the approximation of an optically thin plasma is not applicable. Also, calibration-free LIBS (CF-LIBS) becomes invalid. CF-LIBS allows one to overcome the matrix effect by taking into account the plasma temperature and electron number density, as discussed by Ciucci *et al* [30]. However, when the sample nanoparticles are coated on a high-purity graphite substrate, the concentration of the analytes is much lower. Thus, self-absorption could be neglected, as confirmed in the following section.

Due to self-absorption, the intensity of an emission line is lower than that observed in an optically thin condition. Assuming an optically thin plasma and a local thermodynamic equilibrium (LTE) during signal acquisition, the measured integral line intensity [31]:

$$I_\lambda^{ki} = \frac{hc}{4\pi\lambda_{ki}} A_{ki} L N \frac{g_k}{U_s(T)} \exp\left(- \frac{E_k}{K_B T} \right) \quad (1)$$

where I_λ^{ki} is the intensity of a transition between two energy levels E_k and E_i, h is Planck's constant, c is the speed of light, λ is the transition wavelength, A_{ki} is the transition probability, L is the characteristic length of the plasma, N is the number density, g_k is the degeneracy, $U_s(T)$ is the partition function for the emitting species, k_B is Boltzmann's constant and T is the plasma temperature. For optically thin conditions, the theoretical doublet line intensity ratio of the same species can be expressed as:

$$\frac{I_1}{I_2} = \left(\frac{\lambda_{nm,Z}}{\lambda_{ki,Z}} \right) \left(\frac{A_{ki,Z}}{A_{nm,Z}} \right) \left(\frac{g_{k,Z}}{g_{n,Z}} \right) \exp\left(- \frac{E_{k,Z} - E_{n,Z}}{K_B T} \right) \quad (2)$$

For two emission lines having the same upper level (or as close as possible), the temperature effect of the Boltzmann factor on the reproducibility of the line intensity ratio is minimized. By neglecting the exponential factor under this condition, one can determine the theoretical value of the intensity ratio of the doublet lines by using the inherent atomic parameters of the transitions, which are independent of the experimental parameters. The doublet lines have similar energy level structures and close wavelengths, and their intensities are maximized. Here, the Al I lines at 308.21 and 309.27 nm

were used to determine whether the plasmas from the CMM NCGT were optically thin. **Figure 11** shows the ratio of 308.21–309.27 nm line intensities as a function of the time delay. The line-dot-line represented the ratio of the theoretical transition probabilities, the red circles represent the experimental results, and the error bars represent the RSD of ten duplicate measurements. The experimental and theoretical results were in good agreement within the experimental error range over the entire plasma decay time. In addition, the electron number density at different delay times is also plotted in **Figure 11**. According to the McWhirter criteria [32], this density was sufficient to maintain the plasma in a LTE.

CONCLUSION

High-purity graphite targets are considered to be an ideal matrix for nanoparticle-enhanced LIBS due to their simple spectral structure. Chinese herbal medicine nanoparticles coated on high-purity graphite targets to study the feasibility and capacity. Under optimized experimental conditions, a stable, relatively homogeneous, and approximately optically thin laser-induced breakdown plasma is used to diagnosis the parameters of plasma. Line identifications were greatly simplified and a large improvement in spectral stability was obtained.

DATA AVAILABILITY STATEMENT

Publicly available datasets were analyzed in this study. This data can be found here: https://physics.nist.gov/PhysRefData/ASD/lines_form.html.

AUTHOR CONTRIBUTIONS

WH, DS and MS contributed to the proposition of ideas and experimental design of this study; WH and YW performed the Experimental operation and data processing; WH, DS and MS jointly wrote the article; XL and YY helped perform the general analysis with constructive discussions.

FUNDING

REFERENCES

1. Yi R, Li J, Yang X, Zhou R, Yu H, Hao Z, et al. Spectral Interference Elimination in Soil Analysis Using Laser-Induced Breakdown Spectroscopy Assisted by Laser-Induced Fluorescence. *Anal Chem* (2017) 89:2334–7. doi:10.1021/acs.analchem.6b03969

2. Cahoon EM, Almirall JR. Quantitative Analysis of Liquids from Aerosols and Microdrops Using Laser Induced Breakdown Spectroscopy. *Anal Chem* (2012) 84:2239–44. doi:10.1021/ac202834j

3. Tsai S-JJ, Chen S-Y, Chung Y-S, Tseng P-C. Spatially Resolved, Laser-Induced Breakdown Spectroscopy, Development, and Application for the Analysis of Al and Si in Nickel-Based Alloys. *Anal Chem* (2006) 78:7432–9. doi:10.1021/ac060749d

4. Liu X, Qiao S, Ma Y. Highly Sensitive Methane Detection Based on Light-Induced Thermoelastic Spectroscopy with a 2.33 Mm Diode Laser and Adaptive Savitzky-Golay Filtering. *Opt Express* (2022) 30:1304–13. doi:10.1364/OE.446294

5. Ma Y, Hong Y, Qiao S, Lang Z, Liu X. H-shaped Acoustic Micro-resonator-based Quartz-Enhanced Photoacoustic Spectroscopy. *Opt Lett* (2022) 47:601–4. doi:10.1364/OL.449822

6. Liu X, Ma Y. Sensitive Carbon Monoxide Detection Based on Light-Induced Thermoelastic Spectroscopy with a Fiber-Coupled Multipass Cell [Invited]. *Chin Opt Lett.* (2022) 20:031201. doi:10.3788/COL202220.031201

7. Ma Y, Hu Y, Qiao S, Lang Z, Liu X, He Y, et al. Quartz Tuning forks Resonance Frequency Matching for Laser Spectroscopy Sensing. *Photoacoustics* (2022) 25:100329. doi:10.1016/j.pacs.2022.100329

8. Hohreiter V, Ball AJ, Hahn DW. Effects of Aerosols and Laser Cavity Seeding on Spectral and Temporal Stability of Laser-Induced Plasmas: Applications to LIBS. *J Anal Spectrom* (2004) 19:1289–94. doi:10.1039/b402190h

9. Sun D-X, Su M-G, Dong C-Z. Emission Signal Enhancement and Plasma Diagnostics Using Collinear Double Pulse for Laser-Induced Breakdown Spectroscopy of Aluminum Alloys. *Eur Phys J Appl Phys* (2013) 61:30802. doi:10.1051/epjap/2013120470

10. Li L, Wang Z, Yuan T, Hou Z, Li Z, Ni W. A Simplified Spectrum Standardization Method for Laser-Induced Breakdown Spectroscopy Measurements. *J Anal Spectrom* (2011) 26:2274–80. doi:10.1039/c1ja10194c

11. Hou ZY, Wang Z, Lui SL, et al. Improving data stability and prediction accuracy in laser-induced breakdown spectroscopy by utilizing a combined atomic and ionic line algorithm. *J Anal Spectrom* (2013) 28(1):107–13. doi:10.1039/C2JA30104K

12. Han W, Su M, Sun D, Yin Y, Wang Y, Gao C, et al. Analysis of Metallic Elements Dissolution in the Astragalus at Different Decocting Time by Using LIBS Technique. *Plasma Sci Technol* (2020) 22:085501. doi:10.1088/2058-6272/ab861b

13. Babushok VI, DeLucia FC, Jr, Gottfried JL, Munson CA, Miziolek AW. Double Pulse Laser Ablation and Plasma: Laser Induced Breakdown Spectroscopy Signal Enhancement. *Spectrochimica Acta B: At Spectrosc* (2006) 61:999–1014. doi:10.1016/j.sab.2006.09.003

14. Xiong G, Li S, Tse SD. Tuning Excitation Laser Wavelength for Secondary Resonance in Low-Intensity Phase-Selective Laser-Induced Breakdown Spectroscopy for *In-Situ* Analytical Measurement of Nanoaerosols. *Spectrochimica Acta Part B: At Spectrosc* (2018) 140:13–21. doi:10.1016/j.sab.2017.11.013

15. Harilal SS, Tillack MS, O'Shay B, Bindhu CV, Najmabadi F. Confinement and Dynamics of Laser-Produced Plasma Expanding across a Transverse Magnetic Field. *Phys Rev E* (2004) 69:0264132. doi:10.1103/PhysRevE.69.026413

16. Robledo-Martinez A, Sobral H, Garcia-Villarreal A. Effect of Applied Voltage and Inter-pulse Delay in Spark-Assisted LIBS. *Spectrochimica Acta Part B: At Spectrosc* (2018) 144:7–14. doi:10.1016/j.sab.2018.03.002

17. Dell'Aglio M, Alrifai R, De Giacomo A. Nanoparticle Enhanced Laser Induced Breakdown Spectroscopy (NELIBS), a First Review. *Spectrochimica Acta Part B: At Spectrosc* (2018) 148:105–12. doi:10.1016/j.sab.2018.06.008

18. Popov AM, Colao F, Fantoni R. Enhancement of LIBS Signal by Spatially Confining the Laser-Induced Plasma. *J Anal Spectrom* (2009) 24:602–4. doi:10.1039/b818849a

19. Hou J, Zhang L, Yin W, Zhao Y, Ma W, Dong L, et al. Investigation on Spatial Distribution of Optically Thin Condition in Laser-Induced Aluminum Plasma and its Relationship with Temporal Evolution of Plasma Characteristics. *J Anal Spectrom* (2017) 32:1519–26. doi:10.1039/c7ja00175d

20. Zhou B, Kane TJ, Dixon GJ, Byer RL. Efficient, Frequency-Stable Laser-Diode-Pumped Nd:YAG Laser. *Opt Lett* (1985) 10:62. doi:10.1364/OL.10.000062

21. Cao SQ, Su MG, Min Q, Sun DX, O'Sullivan G, Dong CZ. Spatio-temporally Resolved Spectral Measurements of Laser-Produced Plasma and Semiautomated Spectral Measurement-Control and Analysis Software. *Phys Plasmas* (2018) 25:023304. doi:10.1063/1.5016361

22. Yao S, Zhao J, Xu J, Lu Z, Lu J. Optimizing the Binder Percentage to Reduce Matrix Effects for the LIBS Analysis of Carbon in Coal. *J Anal Spectrom* (2017) 32:766–72. doi:10.1039/C6JA00458J

23. Winefordner JD, Gornushkin IB, Correll T, Gibb E, Smith BW, Omenetto N. Comparing Several Atomic Spectrometric Methods to the Super Stars: Special Emphasis on Laser Induced Breakdown Spectrometry, LIBS, a Future Super star. *J Anal Spectrom* (2004) 19:1061–83. doi:10.1039/b400355c

24. Wang Y, Su M, Sun D, Wu C, Zhang X, Lu Q, et al. Comparative Study of Magnesium and Calcium in Codonopsis Pilosula Samples Detected by CF-LIBS and LCGD-AES. *Microchemical J* (2018) 137:318–23. doi:10.1016/j.microc.2017.11.011

25. Shi J, Cao B, Wang X-W, Aa J-Y, Duan J-A, Zhu X-X, et al. Metabolomics and its Application to the Evaluation of the Efficacy and Toxicity of Traditional Chinese Herb Medicines. *J Chromatogr B* (2016) 1026:204–16. doi:10.1016/j.jchromb.2015.10.014

26. Chan K. Chinese Medicinal Materials and Their Interface with Western Medical Concepts. *J ethnopharmacology* (2005) 96:1–18. doi:10.1016/j.jep.2004.09.019

27. Qian M, Ren C, Wang D, Zhang J, Wei G. Stark Broadening Measurement of the Electron Density in an Atmospheric Pressure Argon Plasma Jet with Double-Power Electrodes. *J Appl Phys* (2010) 107:063303. doi:10.1063/1.3330717

28. Aguilera JA, Aragón C. Multi-element Saha-Boltzmann and Boltzmann Plots in Laser-Induced Plasmas. *Spectrochimica Acta Part B: At Spectrosc* (2007) 62:378–85. doi:10.1016/j.sab.2007.03.024

29. Luque J. LIFBASE: Database and Spectral Simulation Progrm (Versional. 6). SRI Report MP 99-.009 1999.(2021) Available at: http://www.kinetics.nsc.ru/chichinin/databases/Lifbase.pdf.

30. Ciucci A, Corsi M, Palleschi V, Rastelli S, Salvetti A, Tognoni E. New Procedure for Quantitative Elemental Analysis by Laser-Induced Plasma Spectroscopy. *Appl Spectrosc* (1999) 53:960–4. doi:10.1366/0003702991947612

31. Cowan RD, Kim YK. The Theory of Atomic Structure and Spectra. *Phys Today* (1982) 35:57. doi:10.1063/1.2915135

32. Huddlestone RH, Leonard SL, Furth HP. Plasma Diagnostic Techniques. *Phys Today* (1966) 19:94–5. doi:10.1063/1.3048484